GDCh Research Article Angewandte International Edition Chemie www.angewandte.org

How to cite: Angew. Chem. Int. Ed. 2025, e202422726
doi.org/10.1002/anie.202422726

Single-Crystal Cathodes

Mitigating Diffusion-Induced Intragranular Cracking in Single-Crystal $LiNi_{0.5}Mn_{1.5}O_4$ via Extended Solid-Solution Behavior

Hyeonsol Shin[+], Agwu Ndukwe[+], Taemin Kim, Ji Hoon Lee, Guanchen Li,* and Hyeon Jeong Lee**

Abstract: Single-crystal cathodes have been investigated for their inherent resistance to intergranular cracking due to the absence of grain boundaries. However, these materials exhibit significant intragranular cracking, and the underlying mechanisms remain unclear. In this study, we examined the impact of extended solid-solution reactions on mitigating crack formation in magnesium-doped single-crystal $LiNi_{0.5}Mn_{1.5}O_4$ (Mg-SC-LNMO) cathodes. With Mg acting as a structural pillar, the overall volume change was reduced by nearly 50 %, the two-phase reaction was effectively suppressed, and the Li-ion diffusion coefficient was doubled. Continuum modeling based on experimental observations demonstrates that Mg doping significantly reduces the internal stress induced by lithium diffusion, thereby preserving the mechanical integrity of single-crystal LNMO. This improvement leads to enhanced electrochemical performance and durability. Our study provides new insights into mechanically robust single-crystal cathodes and proposes a design strategy to improve the durability of next-generation Li-ion batteries.

Introduction

As the demand for electric vehicles grows, developing Li-ion batteries with high energy density has become increasingly critical.[1] Spinel-type lithium nickel manganese oxide ($LiNi_{0.5}Mn_{1.5}O_4$, LNMO) is a promising cathode material due to its significantly lower cost – approximately 40 % that of lithium nickel cobalt manganese oxide ($LiNi_xCo_yMn_zO_2$ (NMC), $x > 0.8$) – along with its higher operation voltage (5 V vs. Li/Li^+).[2] Because most cathode materials, including LNMO, are synthesized by aggregating nanoscale primary particles into secondary particles, the anisotropic volume change of misoriented primary particles often induces intergranular cracking within these secondary particles.[3] Consequently, single-crystal cathodes without grain boundaries are being actively investigated for their potential to improve mechanical integrity.[4] Although polycrystalline LNMO is less susceptible to intergranular cracking than layered NMC cathodes because of its isotropic dimensional change during charge-discharge, it still experiences intragranular cracking at the primary particle level.[5] During lithium insertion, an inhomogeneous lithium distribution forms, generating mechanical stresses within particles that are particularly problematic at high charging/discharging rates.[6] When this stress induced by lithiation/de-lithiation exceeds the material yield strength, particles crack.[7] To enhance the cyclability of single-crystal LNMO cathodes, various strategies – such as coating, downsizing, and doping – have been investigated.[8] However, the influence of these approaches on stress evolution and mechanical integrity at the particle level is poorly understood. Therefore, a comprehensive understanding of the mechanisms driving intragranular cracking in single crystals is essential for developing design strategies that ensure the durability of LNMO. Continuum models can simulate lithium and stress distributions within particles, capturing aspects that are not directly measurable.[6d] Material properties, including phase mismatch, Poisson's ratio, lithium diffusivity, volume change, surface energy, and interfacial kinetics, as well as particle geometry – such as particle size, shape, and pre-crack geometry – have all been shown to influence stress accumulation and mechanical failure.[9] Therefore, continuum simulations of single-crystal particles can help identify key material parameters that limit the durability and performance of LNMO particles.

In this study, we investigated two types of single-crystal LNMOs: conventional LNMO and LNMO doped with magnesium (Mg). Although both materials share the same crystal structure, their distinct phase evolution behaviors are critical in the formation of intragranular cracks and, consequently, the electrochemical performance of LNMO. Our in situ X-ray diffraction (XRD) and ex situ X-ray absorption fine structure (XAFS) analyses confirmed that Mg acts as a structural pillar, reducing the volume change in LNMO from 5.2 % to 2.65 % and promoting a solid-solution reaction rather than a two-phase reaction at a high potential

[*] H. Shin,[+] T. Kim, Prof. H. J. Lee
Department of Materials Science and Engineering, Ulsan National Institute of Science and Technology (UNIST),
Ulsan 44919, Republic of Korea
E-mail: hyeonjeong.lee@unist.ac.kr

A. Ndukwe,[+] Dr. G. Li
James Watt School of Engineering, University of Glasgow,
Glasgow G12 8QQ, United Kingdom
E-mail: guanchen.li@glasgow.ac.uk

Prof. J. H. Lee
School of Materials Science and Engineering, Kyungpook National University,
Daegu 41566, Republic of Korea
E-mail: jihoonlee@knu.ac.kr

[+] These authors contributed equally to this work

of 4.8 V. Furthermore, the Mg-doped single-crystal LNMO (Mg-SC-LNMO) exhibited a doubled Li-ion diffusion coefficient compared with the undoped single-crystal LNMO (SC-LNMO), facilitating a uniform lithium distribution within the particle without forming a secondary phase throughout the charge–discharge process. Consequently, Mg-SC-LNMO demonstrates robust mechanical integrity even at a high C-rate of 10C, along with stable cycling performance. Continuum modeling of LNMO particles at various C-rates confirmed that Mg doping reduces von Mises stress in Mg-SC-LNMO. Based on these findings, we propose a stress threshold responsible for intragranular cracking in LNMO and define criteria for the lithium diffusivities and volume changes needed to mitigate crack formation at different C-rates. Our results provide insights into stress evolution in single-crystal LNMO and offer material design principles for stress management that may apply to dopants other than Mg. Therefore, this study paves the way for developing more durable and robust single-crystal cathode materials for next-generation Li-ion batteries.

Results and Discussion

Single-crystal $LiNi_{0.5}Mn_{1.5}O_4$ (SC-LNMO) and Mg-doped single-crystal $LiNi_{0.5}Mn_{1.5}O_4$ (Mg-SC-LNMO) were synthesized using a molten salt method (see Experimental section). Because Mg^{2+} and Ni^{2+} share the same oxidation state and have similar ionic radii, Mg doping is not expected to alter the lattice structure significantly.[10] To assess the impact of Mg doping on SC-LNMO properties, Mg concentrations were set at 1, 2, and 4 mol %, with each sample denoted as "Mg-X-SC-LNMO," where X indicates the Mg molar concentration (X = 0.01, 0.02, and 0.04).

Scanning electron microscopy (SEM) images of the SC-LNMO and Mg-SC-LNMO series reveal octahedral particles enclosed by (111) facets with particle sizes ranging from 1 to 3 μm. The SEM images, D_{50} values, and specific surface areas of the Mg-SC-LNMO series confirm that Mg doping does not induce significant changes in particle size or shape (Figures 1a, S1, and Table S1). Energy-dispersive spectroscopy (EDS) elemental mappings confirm the uniform distribution of Mg throughout each particle in the Mg-SC-LNMO series. XRD patterns of both SC-LNMO and Mg-SC-LNMO series exhibit a cubic spinel structure without any rock salt phase ($Li_xNi_{1-x}O$), indicating successful synthesis without impure phases (Figure 1b). Transmission electron microscopy (TEM) measurements of SC-LNMO and Mg-0.02-SC-LNMO showed that the lattice spacing between adjacent fringes was consistently 4.75 Å, corresponding to the (111) plane of the cubic spinel phase (Figure 1c).[11]

Typically, LNMO exhibits two distinct phases based on the distribution of Ni and Mn sites: an "ordered" structure (where Ni^{2+} and Mn^{4+} occupy the 4b and 12d octahedral sites, respectively) and and a "disordered" structure (in which Ni^{2+}, Ni^{3+}, Mn^{3+}, and Mn^{4+} are randomly distributed in the octahedral 16d site).[12] These two crystallographic configurations result in distinct material properties and electrochemical behaviors.[13] To verify the structural characteristics of the SC-LNMO and Mg-SC-LNMO series, Fourier transform infrared (FT-IR) and Raman spectroscopy

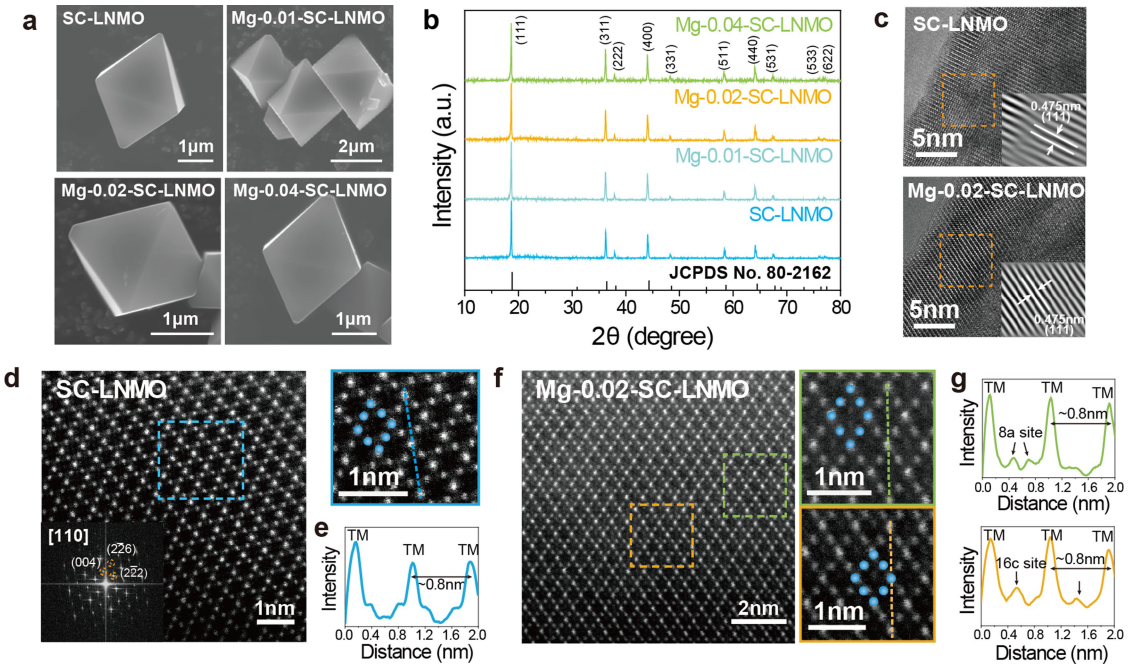

Figure 1. Characterization of the SC-LNMO and Mg-SC-LNMO series. (a) SEM images and (b) XRD patterns of the SC-LNMO and Mg-SC-LNMO series. (c) HR-TEM images with corresponding lattice fringes of SC-LNMO and Mg-0.02-SC-LNMO. (d) HADDF-STEM image of SC-LNMO along [110] with an enlarged image of the ROI. (e) Intensity profile along the blue line. (f) HADDF-STEM image of Mg-0.02-SC-LNMO along [110] with enlarged images of the ROI. (g) Intensity profiles along the green and orange lines.

analyses were performed (Figure S2). In the FT-IR spectra, the peak at 618 cm^{-1} corresponding to the Mn–O vibration band, shows higher intensity than the 574 cm^{-1} peak associated with the Ni–O vibration band, indicating that the crystal structure of both samples resembles the disordered structure of Fd-3 m.[10b,14] Furthermore, all synthesized LNMO samples in this study exhibit five vibration bands at 618, 574, 553, 497, and 458 cm^{-1} in the FT-IR spectra, further confirming their disordered structures (Figure S2a). The weaker and broader FT-IR peaks in the SC-LNMO and Mg-SC-LNMO series, compared to the ordered LNMO sample, indicate lattice distortion attributed to Jahn–Teller effects due to the presence of Mn^{3+}.[15] In the Raman spectra of the SC-LNMO and Mg-SC-LNMO series, characteristic peak splitting near 580–620 cm^{-1}, as well as distinct peaks at 160, 218, and 240 cm^{-1} associated with an ordered structure, were absent (Figure S2b).[16] Thus, Raman analysis confirms that the SC-LNMO and Mg-SC-LNMO series exhibit a disordered structure with Fd-3 m symmetry, consistent with the FT-IR results.

Scanning transmission electron microscopy (STEM) was performed to investigate the atomic structures of SC-LNMO and Mg-0.02-SC-LNMO. High-resolution STEM images of SC-LNMO along the [110] crystallographic analysis revealed a typical spinel structure characterized by a diamond shape with empty 16c octahedral sites at the center, consistent with previous reports (Figures 1d and 1e).[17] In contrast, STEM images of Mg-0.02-SC-LNMO display two distinct diamond-like frameworks: one featuring a center-filled diamond where Mg occupies the previously vacant 16c octahedral site, while the other structure includes a diamond framework with two atoms, indicating partial occupancy of the 8a tetrahedral site by Mg and suggesting partial substitution of Li by Mg (Figure 1f). These distinct atomic arrangements were confirmed by line profiles (Figure 1g). Thus, the introduction of Mg into the LNMO crystal structure increases the occupancy of Mg at the 16c or 8a crystallographic sites, where they act as structural pillars, potentially influencing the electrochemical behavior during charge–discharge processes.[8f,18]

To evaluate the effect of Mg doping, the electrochemical properties of the SC-LNMO and Mg-SC-LNMO series were assessed in a half-cell setup with a moderate active material loading of 4.2 mg cm^{-2} (Figure 2). As displayed in Figure 2a, the Galvanostatic charge–discharge (GCD) curves for both SC-LNMO and Mg-SC-LNMO series exhibit three plateaus

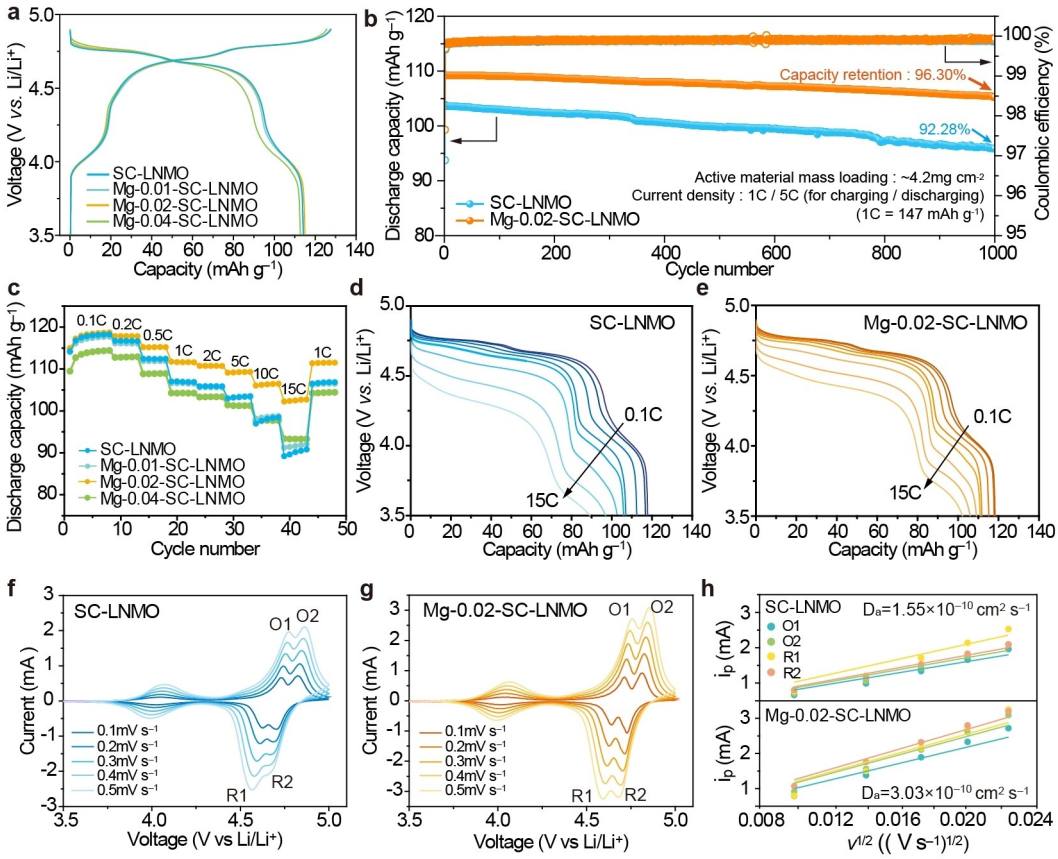

Figure 2. Electrochemical properties of the SC-LNMO and Mg-SC-LNMO series. (a) Galvanostatic charge–discharge (GCD) profiles of the SC-LNMO and Mg-SC-LNMO series at 0.1C (1C = 147 mA g^{-1}). (b) Cycling performances of SC-LNMO and Mg-0.02-SC-LNMO at 1C charge and 5C discharge. (c) Rate performances of the SC-LNMO and Mg-SC-LNMO series. Discharge curves of (d) SC-LNMO and (e) Mg-0.02-SC-LNMO at different rates. Cyclic voltammetry curves of (f) SC-LNMO and (g) Mg-0.02-SC-LNMO at various scan rates. (h) Linear relationship between peak current (i_p) and square root of scan rate ($v^{1/2}$) for SC-LNMO and Mg-0.02-SC-LNMO.

at 4.8, 4.7, and 4 V (vs. Li^+/Li), corresponding to the redox voltage plateaus of $Ni^{4+/3+}$, $Ni^{3+/2+}$, and $Mn^{4+/3+}$, respectively.[12a,19] The substantial capacity attributed to the $Mn^{4+/3+}$ redox reaction indicates a disordered structure of the SC-LNMO and Mg-SC-LNMO series, consistent with the FT-IR and Raman results. SC-LNMO, Mg-0.01-SC-LNMO, and Mg-0.02-SC-LNMO exhibited similar discharge capacities of 114.23, 114.16, and 114.98 $mAh\,g^{-1}$, respectively, at 0.1C, confirming the minimal effect of low Mg concentrations on the discharge capacity. However, Mg-0.04-SC-LNMO delivered a slightly lower discharge capacity of 112.71 $mAh\,g^{-1}$ at the same C rate due to the increased Mg content, which is not redox-active. The cycling performances of the samples were evaluated at various current densities. Under 1C/1C charge–discharge conditions, SC-LNMO, Mg-0.01-SC-LNMO, Mg-0.02-SC-LNMO, and Mg-0.04-SC-LNMO delivered discharge capacities of 105.83, 105.31, 111.2, and 103.73 $mAh\,g^{-1}$, respectively, with comparable capacity retentions of approximately 99 % after 100 cycles (Figure S3). More pronounced impact of Mg on cycling performance was observed under a high discharge rate (Figure 2b). At the 1C/5C charge/discharge condition, Mg-0.02-SC-LNMO showed a discharge capacity of 109.29 $mAh\,g^{-1}$, which is higher than that of SC-LNMO (103.89 $mAh\,g^{-1}$). After 1000 cycles at the same current density, Mg-0.02-SC-LNMO retained 96.3 % of its initial capacity, whereas the SC-LNMO cell retained 92.28 % of its initial capacity. The rate performance confirmed that the Mg content affects the discharge capacity of LNMO at high current densities (Figure 2c). SC-LNMO and Mg-0.01-SC-LNMO exhibited comparable discharge capacities of 90.77 and 92.01 $mAh\,g^{-1}$, respectively, at 15C, representing 79.46 % and 80.6 % of their capacities at 0.1C. Notably, Mg-0.02-SC-LNMO demonstrated an improved discharge capacity of 102.72 $mAh\,g^{-1}$ at 15C, which corresponds to 89.34 % of its capacity at 0.1C. A similar trend was observed in pouch-type cells with larger active areas (Tables S2 and S3), where the Mg-0.02-SC-LNMO electrode delivered a capacity of 114.38 $mAh\,g^{-1}$ at C/3, along with an extended cycle life compared to SC-LNMO (Figure S4).

For clarity, Mg-0.02-SC-LNMO, which exhibits the best electrochemical performance among the Mg-SC-LNMO series, is hereafter referred to as Mg-SC-LNMO. Further evaluations were conducted for both SC-LNMO and Mg-SC-LNMO. The discharge curves of SC-LNMO and Mg-SC-LNMO, measured across current densities from 0.1C to 15C during discharge, are shown in Figures 2d and 2e. SC-LNMO exhibits substantial polarization and capacity decay with increasing current density, while Mg-SC-LNMO maintains lower polarization and higher capacity, confirming that Mg incorporation into the LNMO structure enhances Li-ion diffusion. The redox peak current (I_p) and the square root of the CV scan rate ($v^{1/2}$) exhibit a linear relationship in both SC-LNMO and Mg-SC-LNMO, confirming that the electrochemical processes in both samples are diffusion-controlled (Figures 2f–h).[20] The Li-ion diffusion coefficients for the O1, O2, R1, and R2 peaks, calculated using the Randles-Sevcik equation with CV data, are reported in Table S4. The average diffusion coefficient (D_a) of Mg-SC-LNMO was approximately double that of SC-LNMO, with values of $3.03\times10^{-10}\,cm^2\,s^{-1}$ and $1.55\times10^{-10}\,cm^2\,s^{-1}$, respectively, demonstrating superior lithiation and delithiation kinetics in Mg-SC-LNMO. Notably, the Li-ion diffusion coefficients associated with the Ni^{3+}/Ni^{4+} redox couple (O2 and R2) in Mg-SC-LNMO are significantly higher than those in SC-LNMO, indicating more facile Li-ion diffusion in Mg-SC-LNMO at high potentials above 4.74 V. Because Li-ions are extracted from the 8a sites via the 8a–16c–8a three-dimensional channel in the LNMO, the observation that Mg ions occupying the 16c and 8a sites enhance rather than hinder Li-ion diffusion within the LNMO structure is particularly noteworthy.[21]

To elucidate the origin of enhanced Li-ion diffusion in Mg-SC-LNMO, in situ XRD analysis was conducted during the charge–discharge process at a current of C/8 (Figures 3a and 3b). SC-LNMO and Mg-SC-LNMO exhibited similar GCD curves, as confirmed by electrochemical analyses. During delithiation up to 4.79 V, both samples displayed a solid-solution reaction, evidenced by gradual peak shifts toward higher two-theta values without any XRD peak splitting, consistent with previous reports on disordered LNMO materials.[22] However, the in situ XRD results after further delithiation above 4.79 V revealed clear discrepancies in the structural evolution between the two samples. In SC-LNMO, new XRD peaks at 28.8°, 31.4°, 37.7°, 41.2°, and 43.2° (denoted by a star in Figure S5) were observed, indicating a phase transformation to the fully delithiated phase via a two-phase reaction at high potential (Figure 3a). In sharp contrast, Mg-SC-LNMO maintained solid-solution behavior throughout the charge process, transitioning smoothly from LNMO to $Ni_{0.5}Mn_{1.5}O_4$ (Figure 3b). The shift in the XRD peaks was also more pronounced in SC-LNMO; for example, the (440) peak exhibited a broader range of shift in SC-LNMO than in Mg-SC-LNMO. The lattice volume change, derived from the shift of (111) peaks during charge–discharge, indicated that the lattice volume change ($\Delta V \approx 5.2\,\%$, 539.82 $Å^3 \rightarrow$511.75 $Å^3$) of SC-LNMO was greater than that of Mg-SC-LNMO ($\Delta V \approx 2.65\,\%$, from 535.02 $Å^3 \rightarrow$520.84 $Å^3$). This trend was confirmed by ex situ XRD analysis (Figure S6). As the potential increased from 4.8 V to 4.83 V, SC-LNMO showed a sudden shift in the XRD peaks, stabilizing at 4.9 V, indicating a two-phase reaction (Figures S6a and S6c).[22a] Conversely, Mg-SC-LNMO exhibited a gradual shift in peak positions throughout the charging process up to 4.9 V, supporting the solid-solution behavior of Mg-SC-LNMO during charge–discharge (Figures S6b and S6d). The ex situ XRD analysis also revealed reduced lattice parameter variation in Mg-SC-LNMO. For instance, the (111) peak shifted by 0.36° during the charge process of SC-LNMO (8.133 Å to 7.981 Å), whereas in Mg-SC-LNMO, the (111) peak shifted by 0.20° (8.125 Å to 8.039 Å). The significant differences in peak shifts observed in the XRD analysis can be attributed to the Mg acting as a structural pillar. Based on both the electrochemical properties and the in situ XRD analysis, it is evident that Mg extends the solid-solution behavior and mitigates lattice misfits during charge–discharge, signifi-

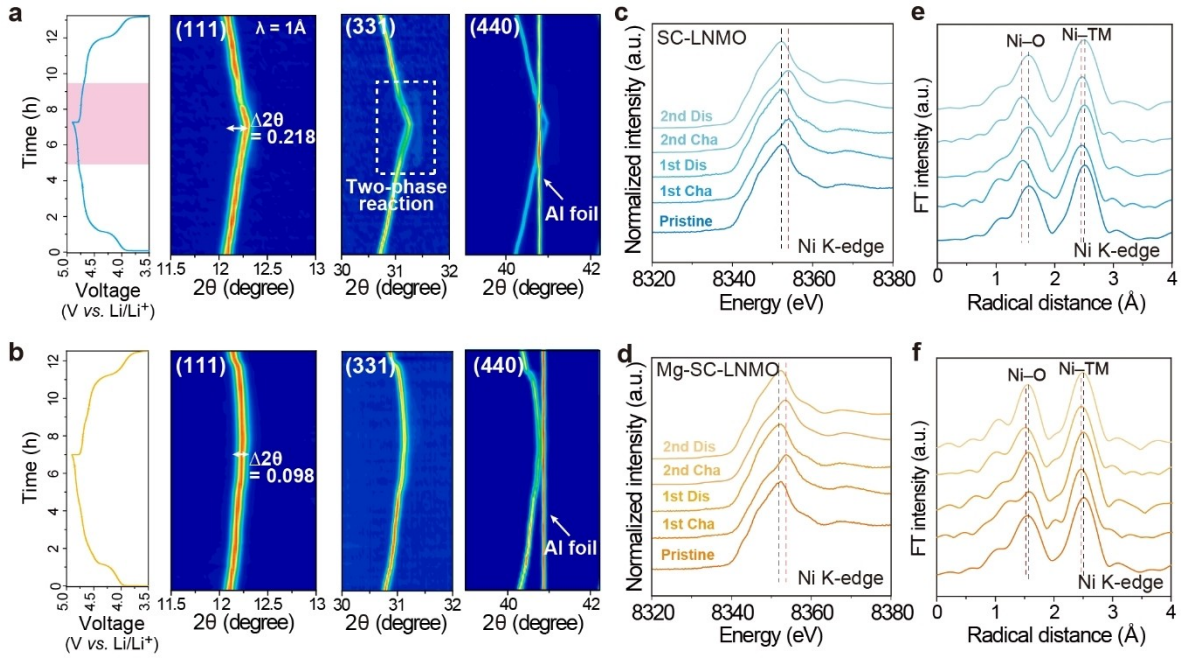

Figure 3. In situ XRD and ex situ XAFS analyses of SC-LNMO and Mg-SC-LNMO. GCD curve at C/8 with contour maps showing the XRD peak evolution of the (111), (331), and (440) reflections for (a) SC-LNMO and (b) Mg-SC-LNMO. XANES profiles at the Ni K-edge at various charge–discharge states for (c) SC-LNMO and (d) Mg-SC-LNMO. EXAFS profiles at the Ni K-edge at different charge–discharge states for (e) SC-LNMO and (f) Mg-SC-LNMO.

cantly lowering kinetic barriers and thereby enhancing the rate performance of Mg-SC-LNMO.[23]

To further investigate local structure changes, ex situ X-ray absorption fine structure (XAFS) analysis at the Mn and Ni K-edges was conducted on a series of electrodes in both as-synthesized and various charged states. The E_0 values measured at the Mn K-edge for the as-synthesized SC-LNMO (6550.05 eV) and Mg-SC-LNMO (6550.08 eV) were identical and positioned between those of Mn_2O_3 (6544.44 eV) and MnO_2 (6552.52 eV) references (Figure S7). This confirms that Mn exists in both samples as Mn^{3+} and Mn^{4+}, supporting the disordered structure observed in the FT-IR and Raman analyses. Similarly, the Ni K-edge XANES spectra of both samples were also identical (8341.96 eV for SC-LNMO and 8341.78 eV for Mg-SC-LNMO). The E_0 values of the NiO and $LiNiO_2$ references were 8341.33 and 8342.05 eV, respectively, thus supporting presence of Ni^{2+} and Ni^{3+} in both materials (Figure S8). Both SC-LNMO and Mg-SC-LNMO exhibited substantial shifts in their X-ray absorption near-edge structure (XANES) profiles at the Ni K-edge, with the E_0 value increasing to 8342.62 eV, which is higher than that of Ni^{3+}. This indicates that Ni ions act as the primary redox centers responsible for most of the observed capacity (Figures 3c and 3d). The E_0 values of both Ni and Mn decreased reversibly during the discharge process, and this reversibility persisted across cycles for both samples (Figure S9). Despite similar trends in the E_0 profiles during the charge-discharge process, the extended X-ray absorption fine structure (EXAFS) analysis revealed a significant difference in Ni–O bond length variations between SC-LNMO and Mg-SC-LNMO (Figure S10 and Tables S5–S8). In Mg-SC-LNMO, the Ni–O bond length remained relatively constant throughout charging and discharging, whereas in SC-LNMO, the Ni–O bond length decreased and increased cyclically, indicating that local structural changes in the Ni–O bond significantly affected the lattice volume of SC-LNMO at the bulk scale (Figures 3e and 3f).

Comprehensive XRD and XAFS analyses confirmed that Mg within the LNMO lattice plays a crucial role in (1) extending solid-solution reaction and (2) mitigating structural changes at both bulk and local scales during charge and discharge. These effects reduce phase boundary dislocations, enhance Li-ion diffusion, and minimize strain evolution, potentially improving the mechanical integrity of LNMO particles.

The introduction of Mg into SC-LNMO becomes particularly impactful in thicker electrodes, where high-loading increases mechanical strain and stress accumulation, leading to a higher incidence of cracks and exfoliation during charge-discharge cycles.[24] This stress-induced pulverization accelerates capacity degradation in SC-LNMO.[25] The cycling performances of the high-loading SC-LNMO and Mg-SC-LNMO electrodes with an active material loading of 18 mg cm^{-2}, is shown in Figures 4a and 4b. After 200 cycles at a rate of 1C, the capacity retention of SC-LNMO and Mg-SC-LNMO was 10.1 % and 82.2 %, respectively, indicating that Mg doping significantly enhances capacity retention under high-loading conditions (Figure 4b). To confirm that the observed degradation in SC-LNMO originated from the cathode material rather than the lithium metal or electrolyte, the cycled SC-LNMO cell was disassembled in a glove

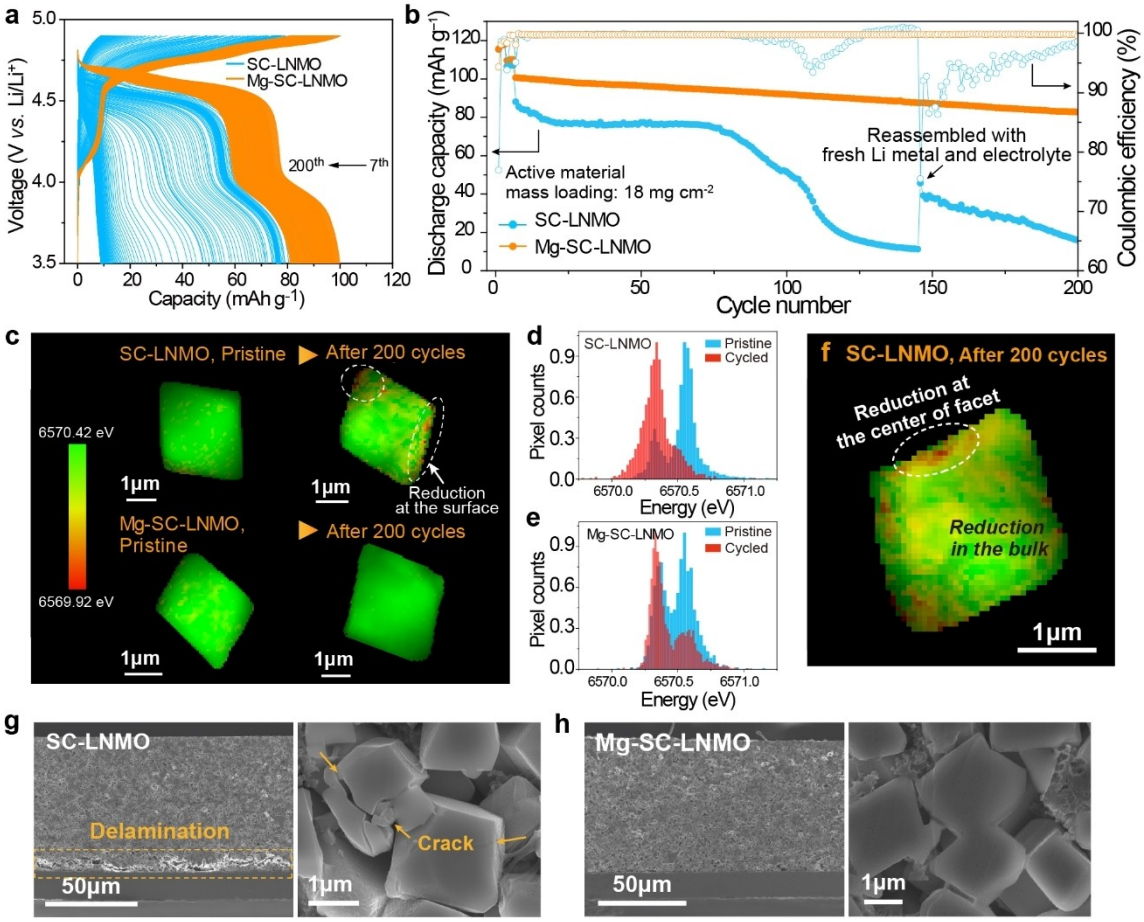

Figure 4. Mechanical failure in SC-LNMO and enhanced cycling stability of Mg-SC-LNMO. (a) GCD curves and (b) cycling performances of high-mass-loading SC-LNMO and Mg-SC-LNMO at 1C and 25 °C. (c) XANES mappings of SC-LNMO and Mg-SC-LNMO at pristine and after 200 cycles. Corresponding histograms for (d) SC-LNMO and (e) Mg-SC-LNMO. (f) Magnified XANES mapping image of SC-LNMO after 200 cycles. Cross-sectional SEM images of high-mass-loading electrodes after 200 cycles for (g) SC-LNMO and (h) Mg-SC-LNMO.

box and reassembled with fresh electrolyte and lithium metal. The discharge capacity of SC-LNMO did not recover after reassembly, confirming that the capacity loss stemmed from the degradation of the cathode material.[26] To examine the impact of Mg on LNMO structural integrity, further analyses were performed on electrodes from cells cycled with SC-LNMO and Mg-SC-LNMO.

Transmission X-ray microscopy (TXM)-XANES mapping confirmed the distribution of Mn valence states within cycled SC-LNMO and Mg-SC-LNMO (Figure 4c). The Mn valence states in the as-synthesized SC-LNMO and Mg-SC-LNMO samples were identical, showing a white line maximum at 6561 eV, consistent with the XANES results presented in Figure S11. After 200 cycles, however, the reduced Mn valence state was significantly more pronounced in SC-LNMO than in Mg-SC-LNMO (Figures 4c–e). This finding supports that the mechanically unstable cathode-electrolyte interphase (CEI) layer in SC-LNMO, caused by repeated volume changes, accelerates TM dissolution (Figure S12).[26a,27] Ex situ STEM and electrochemical impedance spectroscopy (EIS) analyses confirmed that the surface structural transition from spinel to the rocksalt structure was significantly more pronounced in SC-LNMO after cycling (Figures S13–S15 and Table S9). Additionally, TXM-XANES analysis further provided insights into stress evolution in LNMO single crystals, revealing a decrease in Mn oxidation state from the facet centers toward the bulk (Figure 4f), suggesting stress accumulation due to Li-ion diffusion and consequent mechanical degradation in this direction.

Ex situ cross-sectional SEM analysis after 200 cycles at 1C was used to verify the failure origins in the LNMO thick electrodes (Figures 4g and 4 h). Mg-SC-LNMO maintained stable octahedral particle structures, whereas SC-LNMO showed severe particle cracking and electrode delamination. This delamination was attributed to the accumulation of shear stress at the interface, which resulted from substantial volume changes in the SC-LNMO electrode.[28] Furthermore, intragranular cracking in SC-LNMO was observed at the center of the facets, consistent with the TXM-XANES results, indicating that Mg doping enhances particle mechanical integrity. This enhancement is likely due to improved Li-ion diffusion and reduced volume change via an extended

solid-solution reaction, which mitigates the internal stress within the single crystal.

To highlight the effect of diffusion-induced stress on the mechanical deformation of single crystal particles, stress evolution in octahedral particles (Figure 5a) of SC-LNMO and Mg-SC-LNMO was simulated across a range of charging–discharging rates. The simulation parameters are detailed in Table S10. The characteristic diffusion time, τ, is calculated as $\tau = a^2/D$. For a lithium diffusivity of 1.55×10^{-14} $m^2 s^{-1}$, derived from CV results in Figure 2h, a 1 μm LNMO particle has a characteristic time of 65 s. Using the surface lithium flux (J_s), the maximum concentration difference within a particle, $\Delta c = aJ_s/D$, can be estimated to be approximately 70 mol m^{-3} at 1C, translating to an occupancy difference of approximately 0.3 %. Due to this minimal occupancy variation, concentration-dependent properties within the particles, such as lithium diffusivity, can be considered uniform. The inelastic volume changes of SC-LNMO and Mg-SC-LNMO due to delithiation (ε_c) were measured at 4.25, 4.74, 4.8, 4.83, 4.86, and 4.9 V during 0.1C charging by ex situ XRD (Figures 5b, S16, and Table S11). Across the entire charging process, Mg-SC-LNMO exhibited smaller inelastic volume changes than SC-LNMO, indicating that Mg doping stabilized the crystal structure at all lithium contents. Significantly, by extending solid-solution behavior and preventing phase transitions between 4.8 V and 4.9 V, Mg-SC-LNMO reduces the volume change in this range from approximately 2 % in SC-LNMO to approximately 1 %. The time evolution of the maximum von Mises stress throughout the charging process is shown in Figure 5c, correlating with the derivative of the inelastic volume change displayed in Figure 5b, which reflects the lithium

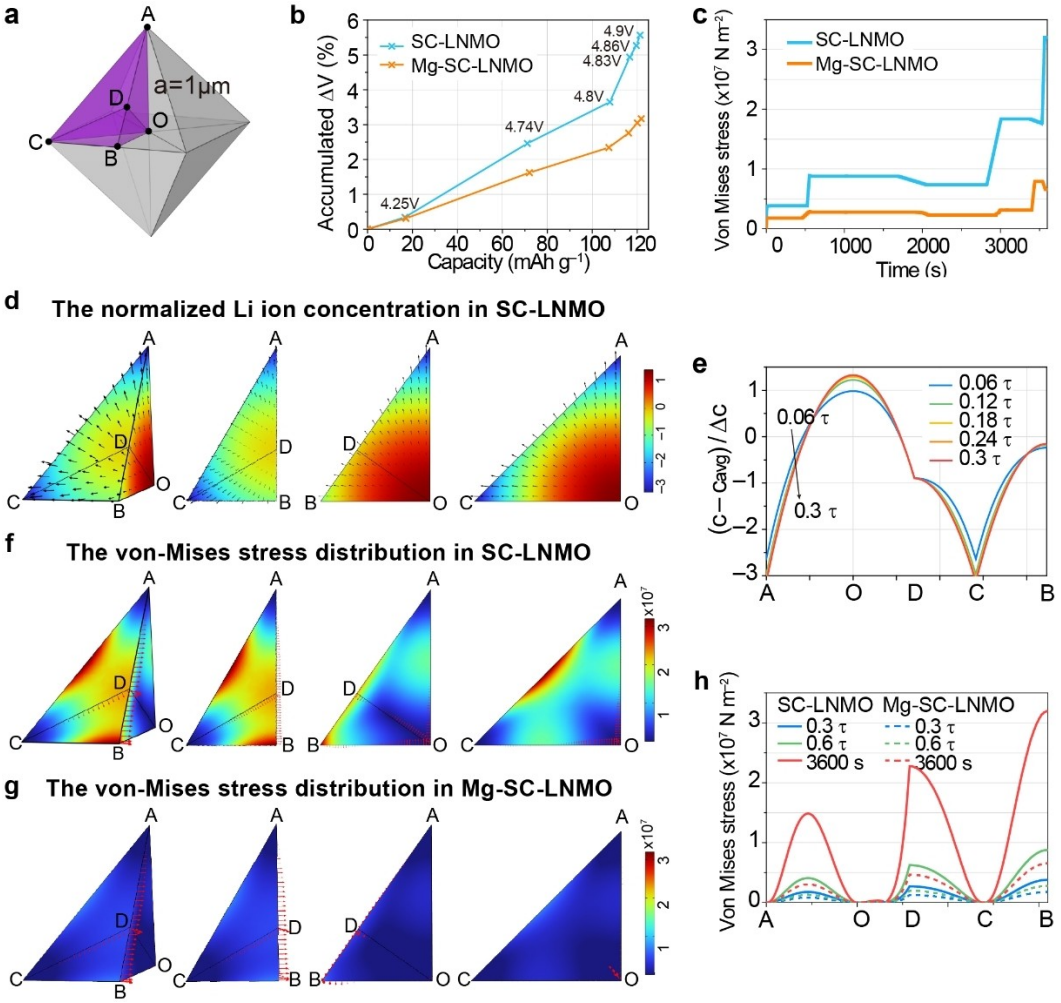

Figure 5. Continuum modeling of the Li concentration and stress evolution in SC-LNMO. (a) Single crystal particle (gray) and simulated region (purple), with points A and C at the two corners, B at the midpoint of the edge, D at the center of the outer surface, and O at the particle center. The length of AO was set to $a = 1$ μm. (b) Pure inelastic volume changes in SC-LNMO and Mg-SC-LNMO due to delithiation. (c) Time evolution of maximum von Mises stress during a 1C charging process. (d) Normalized lithium concentration in SC-LNMO particles at the end of 1C charging, shown in ABC, AOB, and AOC cutting planes. Black arrows indicate lithium flux. (e) Normalized lithium concentration in an SC-LNMO particle along the A–O–D–C-B path at times 0.6 τ, 0.12 τ, 0.18 τ, 0.24 τ, and 0.3 τ during 1C charging. Von Mises stress in an (f) SC-LNMO and (g) Mg-SC-LNMO particle at the end of 1C charging, shown in ABC, AOB, and AOC cutting planes. Red arrows indicate edge traction. (h) Von Mises stress along the path A–O–D–C-B at times 0.3 τ, 0.6 τ, and 3600 s during charging.

partial molar volume $\overline{V}_{Li} = \frac{d\varepsilon_c}{dc}$ at different states of charge (SOC). The maximum von Mises stress aligns with the large volume change between 4.8 V and 4.9 V, and in Mg-SC-LNMO, this stress is approximately 20 % of that in SC-LNMO (Figure 5c). The lithium distributions in the SC-LNMO and Mg-SC-LNMO at the end of the 1C charging process are illustrated in Figures 5d and S17. The dimensionless concentration, $\tilde{c} = (c - \overline{c})/\Delta c$, is plotted, where $\tilde{c}$ represents the volumetric average lithium concentration of the particle. Both particles had a minimum lithium concentration at the corners and a maximum lithium concentration at the center. Figure 5e shows the $\tilde{c}$ values along path A–O–D–C–B at five different times. Similar to diffusion in spherical particles,[6d,29] the $\tilde{c}$ distribution reaches steady state rapidly, in about 0.2 $\tau = 13$ s, which is notably shorter than the charging–discharging period, which spans from minutes to hours. The corner (point A) exhibits the maximum concentration gradient and largest lithium flux, whereas the flux vanishes at the particle center.

The von Mises stress distribution within the SC-LNMO particle at the end of the 1C charging process is illustrated in Figure 5f. The surface cutline AB undergoes tensile stress during delithiation and compressive stress during lithiation, while the particle core (point O) experiences high compressive pressure during delithiation, consistent with previous findings regarding surface and core stresses.[8e] The maximum von Mises stress occurred at the edge midpoint (point B), aligning well with experimental observations show in Figure 4f. TXM-XANES results show substantial Mn reduction at the edge midpoint, which implies diffusion-induced stress in this region may cause cracking and is responsible for TM dissolution. Figure 5h also shows another von Mises stress peak at the face center (point D), which might be another region prone to crack. Because most materials exhibit significantly higher yield stress in compression than in tension,[6d] SC-LNMO single crystal particles are likely to fracture under tensile stress, suggesting that they may crack at the end of the charging process.

To verify the effect of C-rate on crack formation, SC-LNMO and Mg-SC-LNMO were examined by ex situ SEM after 10, 20, and 50 cycles at 1C, 5C, and 10C (Figures 6a and S18). For SC-LNMO, no cracks were observed at 1C, even after 50 cycles; however, substantial crack formation was evident after 20 cycles at 5 and 10C. In contrast, Mg-SC-LNMO displayed no cracks under any tested C-rate or cycling condition. According to our modeling, the lithium diffusivity and volume change appear the two key factors that determine the maximum stress and current density that can induce crack formation. For an analytical analysis, we combined the governing equations (Equations S1–S4) and derived a relationship describing how the maximum von Mises stress $(\sigma_{v,max})$ depends on the C-rate (C), lithium

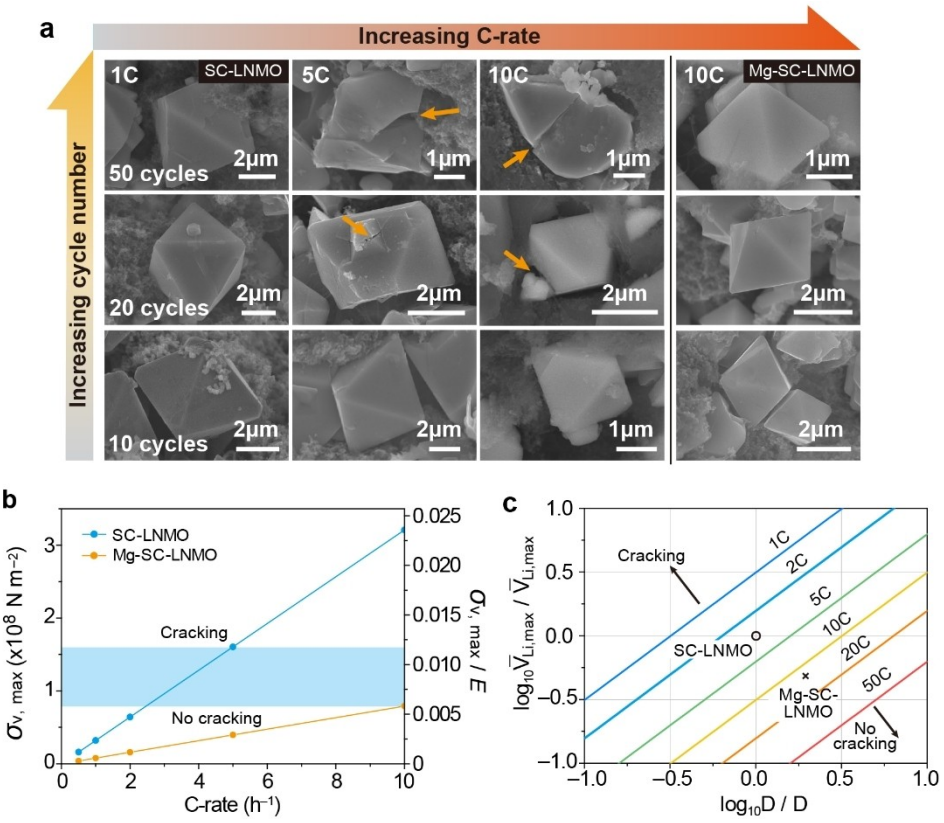

Figure 6. Guidelines for designing SC-LNMOs to mitigate mechanical failures. (a) Ex situ SEM images of SC-LNMO and Mg-SC-LNMO electrodes after cycling at various C-rates. (b) Simulated maximum von Mises stress $(\sigma_{v,max})$ and its ratio to Young's Modulus$(\sigma_{v,max}/E)$ for SC-LNMO and Mg-SC-LNMO at different C-rates. (c) Failure currents of materials with differing diffusivities and partial lithium molar volumes.

partial molar volume ($\overline{V}_{Li}$), diffusivity (D), and Young's modulus (E). An additional term f accounts for the effect of the stress distribution, which is controlled by the lithium flux distribution, particle geometry, and Poisson's ratio:

$$\ln\frac{\sigma_{V,max}}{E} = \ln C + \ln\overline{V}_{Li} - \ln D + f$$

For particles with fixed Poisson's ratio and geometry, f becomes constant once the lithium flux achieves time invariance.

Ex situ XRD results for SC-LNMO and Mg-SC-LNMO during charging at 0.1C confirm that Mg doping reduces the volume change across the full range of lithium occupancy (Figures 5b, S16 and Table S11). Specifically, the maximum $\overline{V}_{Li}$ in SC-LNMO reaches $9.35\times10^{-6}\,m^3\,mol^{-1}$ between 4.8 V and 4.9 V, where a two-phase reaction occurs. Mg doping reduces this maximum $\overline{V}_{Li}$ by more than 50 %.

The von Mises stress was analyzed in conjunction with Young's modulus, reflecting that the failure stress typically scaled with Young's modulus.[9e,30] Since the simulated LNMO particle is a single crystal, characterized by no visible pre-cracks or grain boundaries, the failure process predominantly involves crack initiation rather than propagation.[31] Consequently, a critical stress threshold is incorporated into this model. The maximum von Mises stress of SC-LNMO and Mg-SC-LNMO at different C-rates is shown in Figure 6b. Notably, Mg-SC-LNMO at 10C exhibits a lower maximum von Mises stress than SC-LNMO at 3C, which is consistent with experimental observations where SC-LNMO begins to crack at 5C and 10C, while Mg-SC-LNMO remains crack-free even at 10C. By combining simulation and experimental observations of failure, our study suggests that the critical von Mises stress lies between 80 and 150 MPa, as indicated by the shaded region in Figure 6b. This range aligns with the common yield strength values of electrode materials, typically 0.2 %–1 % of Young's modulus.[6d,30b]

Based on these findings, we simulated materials with various combinations of lithium diffusivity and partial molar volume under a critical von Mises stress of 100 MPa, identifying their maximum C-rate without crack formation. This simulation provides a design principle for producing durable particles for the target C-rate (Figure S19). Figure 6c presents the contours of the failure C-rates across this material search space, demonstrating that electrode materials with higher diffusivity and lower lithium partial molar volume can withstand higher currents. The failure current of Mg-SC-LNMO is expected to be approximately four times higher than that of SC-LNMO, which is attributed to the doubled lithium diffusivity and the 50 % reduction in maximum $\overline{V}_{Li}$ in Mg-SC-LNMO. Extending these results allows us to estimate the lithium diffusivity needed for an LNMO single crystal to remain crack-free at a given C rate. For instance, to ensure stable performance at 20C, an LNMO particle requires an enhanced diffusivity of $6\times10^{-14}\,m^2\,s^{-1}$ or a reduced volume change of 1.6 %.

Conclusion

In summary, we demonstrated that Mg serves as a structural pillar in Mg-SC-LNMO, facilitating solid-solution reactions the entire charge–discharge process. This enhancement in solid-solution behavior significantly improved lithium diffusivity, effectively reducing stress levels within the LNMO single crystal and achieving a high areal capacity of $1.5\,mAh\,cm^{-2}$ with a capacity retention of 82.2 % after 200 cycles at 1C.

Through a detailed analysis of the mechanisms underlying intragranular crack formation in SC-LNMO, using continuum modeling, TMX-XANES, and ex situ SEM, we identified the mid-edge of SC-LNMO as the area experiencing the highest stress, acting as a hotspot for crack initiation. The combined effects of reduced volume change and increased lithium diffusivity due to the solid-solution reaction in Mg-SC-LNMO reduced stress by approximately 80 % compared to SC-LNMO, thereby preventing crack formation even at high C-rates of 10C.

This study provides new insights into the strategic use of dopants to mitigate particle cracking and outlines a design strategy for single-crystal cathode materials to maintain mechanical integrity across a range of C-rates, ultimately advancing the development of more resilient battery systems.

Supporting Information

The authors have cited additional references within the Supporting Information.[32,33,34,35,36]

Acknowledgements

This study was supported by the National Research Foundation of Korea (RS-2024-00345331 and NRF-2022R1C1C1004171). The authors thank UCRF (UNIST Central Research Facilities) for providing equipment support. AN thank the EPSRC Doctoral Training Partnership for financial support. GL and AN thank the University of Glasgow for providing computational support and software. The authors also acknowledge technical supports with 1D (KIST-PAL XRS), 8C (XAFS), 7C (XNI), 6D (XAFS) beamlines of the Pohang Light Source-II in the Pohang Accelerating Laboratory.

Conflict of Interest

The authors declare no conflict of interest.

Data Availability Statement

The data that support the findings of this study are available in the supplementary material of this article.

Keywords: Lithium-ion batteries · Single-crystal cathodes · Cracking · Phase transitions · Diffusion-induced stress

[1] J. W. Choi, D. Aurbach, *Nat. Rev. Mater.* **2016**, *1*, 1–16.

[2] a) J. Jin, J. Wei, Z. Zhou, Z. Xie, *RSC Adv.* **2023**, *13*, 12394–12401; b) Z. Chen, R. Zhao, P. Du, H. Hu, T. Wang, L. Zhu, H. Chen, *J. Mater. Chem. A* **2014**, *2*, 12835–12848; c) H. J. Lee, Z. Brown, Y. Zhao, J. Fawdon, W. Song, J. H. Lee, J. Ihli, M. Pasta, *Chem. Mater.* **2021**, *33*, 1238–1248.

[3] a) X. Cheng, Y. Li, T. Cao, R. Wu, M. Wang, H. Liu, X. Liu, J. Lu, Y. Zhang, *ACS Energy Lett.* **2021**, *6*, 1703–1710; b) P. Yan, J. Zheng, M. Gu, J. Xiao, J.-G. Zhang, C.-M. Wang, *Nat. Commun.* **2017**, *8*, 14101; c) U. H. Kim, H. H. Ryu, J. H. Kim, R. Mücke, P. Kaghazchi, C. S. Yoon, Y. K. Sun, *Adv. Energy Mater.* **2019**, *9*, 1803902; d) Z. Hao, H. Sun, Y. Ni, G. Yang, Z. Yang, Z. Hao, R. Wang, P. Yang, Y. Lu, Q. Zhao, W. Xie, Z. Yan, W. Zhang, J. Chen, *Adv. Mater.* **2024**, *36*, 2307617.

[4] a) J. Sun, X. Cao, H. Yang, P. He, M. A. Dato, J. Cabana, H. Zhou, *Angew. Chem. Int. Ed.* **2022**, *61*, e202207225; b) J. Langdon, A. Manthiram, *Energy Storage Mater.* **2021**, *37*, 143–160.

[5] a) P. Zuo, P. Badami, S. E. Trask, D. P. Abraham, C. Wang, *Small* **2024**, *20*, 2306807; b) S. Liu, X. Liu, D. Ren, T. Li, L. Yi, W. Liu, J. Xu, T. Tan, J. Zhang, Y. Hou, *Nano Energy* **2024**, *121*, 109215; c) C.-H. Jo, N. Voronina, S.-T. Myung, *Energy Storage Mater.* **2022**, *51*, 568–587.

[6] a) D. Alikin, K. Romanyuk, B. Slautin, D. Rosato, V. Y. Shur, A. Kholkin, *Nanoscale* **2018**, *10*, 2503–2511; b) Y. Zhang, Z. Yang, C. Tian, *J. Mater. Chem. A* **2019**, *7*, 23628–23661; c) A. Sengupta, A. Kumar, G. Barik, A. Ahuja, J. Ghosh, H. Lohani, P. Kumari, T. K. Bhandakkar, S. Mitra, *Small* **2023**, *19*, 2206248; d) J. Christensen, J. Newman, *J. Solid State Electrochem.* **2006**, *10*, 293–319.

[7] C. Yuan, W. Lu, J. Xu, *Energy Storage Mater.* **2023**, *60*, 102834.

[8] a) Y. Han, Y. Lei, J. Ni, Y. Zhang, Z. Geng, P. Ming, C. Zhang, X. Tian, J. L. Shi, Y. G. Guo, *Small* **2022**, *18*, 2107048; b) X. Jin, Y. Han, Z. Zhang, Y. Chen, J. Li, T. Yang, X. Wang, W. Li, X. Han, Z. Wang, *Adv. Mater.* **2022**, *34*, 2109356; c) X. Ou, T. Liu, W. Zhong, X. Fan, X. Guo, X. Huang, L. Cao, J. Hu, B. Zhang, Y. S. Chu, *Nat. Commun.* **2022**, *13*, 2319; d) N. R. Park, Y. Li, W. Yao, M. Zhang, B. Han, C. Mejia, B. Sayahpour, R. Shimizu, B. Bhamwala, B. Dang, *Adv. Funct. Mater.* **2024**, *34*, 2312091; e) D. Mao, Z. Fan, L. Song, P. Zhang, J. Xie, S. Su, G. Liu, H. Wang, W. Chu, *Nano Energy* **2024**, *121*, 109231; f) X. Gao, F. Hai, W. Chen, Y. Yi, J. Guo, W. Xue, W. Tang, M. Li, *Small Methods* **2024**, 2301759; g) P. Stüble, H. Geßwein, S. Indris, M. Müller, J. R. Binder, *J. Mater. Chem. A* **2022**, *10*, 9010–9024.

[9] a) S. S. Pandurangi, D. S. Hall, C. P. Grey, V. S. Deshpande, N. A. Fleck, *J. Electrochem. Soc.* **2023**, *170*, 050531; b) M. Zhu, J. Park, A. M. Sastry, *J. Electrochem. Soc.* **2012**, *159*, A492; c) S. Golmon, K. Maute, S.-H. Lee, M. L. Dunn, *Appl. Phys. Lett.* **2010**, *97*; d) K. Zhao, M. Pharr, J. J. Vlassak, Z. Suo, *J. Appl. Phys.* **2010**, *108*; e) Y.-T. Cheng, M. W. Verbrugge, *J. Appl. Phys.* **2008**, *104*; f) Y.-T. Cheng, M. W. Verbrugge, *J. Electrochem. Soc.* **2010**, *157*, A508; g) X. Zhang, A. M. Sastry, W. Shyy, *J. Electrochem. Soc.* **2008**, *155*, A542; h) X. Zhang, W. Shyy, A. M. Sastry, *J. Electrochem. Soc.* **2007**, *154*, A910; i) K. E. Aifantis, S. Hackney, J. Dempsey, *J. Power Sources* **2007**, *165*, 874–879.

[10] a) Y. Wang, G. Du, D. Han, W. Shi, J. Deng, H. Li, W. Zhao, S. Ding, Q. Su, B. Xu, *J. Energy Chem.* **2024**, *91*, 670–679; b) F. Lin, J. Guo, L. Wang, Y. Zhou, H. Wu, D. Zhou, *Electrochim. Acta* **2021**, *399*, 139433.

[11] a) W. Huang, M. Zhang, T. Liu, W. Zhao, L. He, L. Yin, Z. Tan, C. Lin, J. Liu, Q. Zhao, *Nano Energy* **2021**, *89*, 106457; b) C. Khotimah, F.-M. Wang, M. Wohlfahrt-Mehrens, J.-K. Chang, J.-Y. Lin, C.-C. Chang, R. A. Yuwono, S. A. Pradanawati, N.-H. Yeh, C.-C. Hsu, *ACS Sustainable Chem. Eng.* **2023**, *11*, 4374–4388.

[12] a) G. Liang, V. K. Peterson, K. W. See, Z. Guo, W. K. Pang, *J. Mater. Chem. A.* **2020**, *8*, 15373–15398; b) X.-Y. Feng, W.-T. Wu, Q.-Q. Huang, Y.-C. Liu, C. Ni, Z.-M. Huang, X. Liang, C.-H. Chen, H.-F. Xiang, *J. Alloys Compd.* **2023**, *948*, 169768.

[13] S. Sun, X. Li, C. Zhang, X. Wang, J. Wang, C. Wang, Z. J. Xu, Z. Cheng, Y. Bai, *Adv. Mater.* **2024**, 2405876.

[14] Y. Luo, H. Li, T. Lu, Y. Zhang, S. S. Mao, Z. Liu, W. Wen, J. Xie, L. Yan, *Electrochim. Acta* **2017**, *238*, 237–245.

[15] a) F. U. Okudur, J. D'Haen, T. Vranken, D. De Sloovere, M. Verheijen, O. Karakulina, A. Abakumov, J. Hadermann, M. K. Van Bael, A. Hardy, *RSC Adv.* **2018**, *8*, 7287–7300; b) J. Lin, X. Chen, E. Fan, X. Zhang, R. Chen, F. Wu, L. Li, *eScience* **2023**, *3*, 100110.

[16] a) X. Zhang, F. Cheng, K. Zhang, Y. Liang, S. Yang, J. Liang, J. Chen, *RSC Adv.* **2012**, *2*, 5669–5675; b) S. L. Spence, Z. Xu, S. Sainio, D. Nordlund, F. Lin, *Inorg. Chem.* **2020**, *59*, 10591–10603.

[17] M. Lin, L. Ben, Y. Sun, H. Wang, Z. Yang, L. Gu, X. Yu, X.-Q. Yang, H. Zhao, R. Yu, *Chem. Mater.* **2015**, *27*, 292–303.

[18] a) B. Kang, H. Kim, M. Kim, D. Kim, M. Cho, *J. Mater. Chem. A* **2021**, *9*, 26820–26828; b) G. Liang, Z. Wu, C. Didier, W. Zhang, J. Cuan, B. Li, K. Y. Ko, P. Y. Hung, C. Z. Lu, Y. Chen, *Angew. Chem.* **2020**, *132*, 10681–10689.

[19] T. Fu, D. Lu, Z. Yao, Y. Li, C. Luo, T. Yang, S. Liu, Y. Chen, Q. Guo, C. Zheng, *J. Mater. Chem. A* **2023**, *11*, 13889–13915.

[20] Y. L. Shi, N. Wu, M. F. Shen, Y. L. Cui, L. Jiang, Y. H. Qiang, Q. C. Zhuang, *ChemElectroChem* **2014**, *1*, 645–654.

[21] a) D.-w. Kim, H. Shiiba, K. Teshima, N. Zettsu, *J. Mater. Chem. A* **2023**, *11*, 838–848; b) T. Fu, D. Lu, Z. Yao, Y. Li, C. Luo, T. Yang, S. Liu, Y. Chen, Q. Guo, C. Zheng, W. Sun, *J. Mater. Chem. A* **2023**, *11*, 13889–13915; c) J. He, G. Melinte, M. S. D. Darma, W. Hua, C. Das, A. Schökel, M. Etter, A.-L. Hansen, L. Mereacre, U. Geckle, T. Bergfeldt, Z. Sun, M. Knapp, H. Ehrenberg, J. Maibach, *Adv. Funct. Mater.* **2022**, *32*, 2207937.

[22] a) A. Bhatia, C. Leviel, M. Hallot, J. P. Pereira-Ramos, C. Lethien, P. Roussel, R. Baddour-Hadjean, *Adv. Mater. Interfaces* **2022**, *9*, 2200733; b) J. He, G. Melinte, M. S. D. Darma, W. Hua, C. Das, A. Schökel, M. Etter, A. L. Hansen, L. Mereacre, U. Geckle, *Adv. Funct. Mater.* **2022**, *32*, 2207937; c) Y. Han, Y.-S. Jiang, Y. Xia, L. Deng, L.-F. Que, F.-D. Yu, Z.-B. Wang, *Nano Energy* **2022**, *91*, 106636.

[23] a) T. Jin, P. F. Wang, Q. C. Wang, K. Zhu, T. Deng, J. Zhang, W. Zhang, X. Q. Yang, L. Jiao, C. Wang, *Angew. Chem.* **2020**, *132*, 14619–14624; b) J. Xiao, X. Yu, J. Zheng, Y. Zhou, F. Gao, X. Chen, J. Bai, X.-Q. Yang, J.-G. Zhang, *J. Power Sources* **2013**, *242*, 736–741; c) Y. Xue, Y. Han, H.-X. Yu, J. Shu, Z.-B. Wang, L.-L. Zheng, Y.-F. Xia, *Electrochim. Acta* **2018**, *281*, 24–30.

[24] a) Y. Kim, M. Kim, T. Lee, E. Kim, M. An, J. Park, J. Cho, Y. Son, *Electrochem. Commun.* **2023**, *147*, 107437; b) Y. Jung, S. Lee, D. Kim, H. Lee, S. Kim, J. Cho, H. Jin, Y. Kim, J.-S. Park, W.-G. Lee, *J. Power Sources* **2024**, *592*, 233960.

[25] T. Tian, L. L. Lu, Y. C. Yin, Y. H. Tan, T. W. Zhang, F. Li, H. B. Yao, *Small* **2022**, *18*, 2106898.

[26] a) W. Li, Y.-G. Cho, W. Yao, Y. Li, A. Cronk, R. Shimizu, M. A. Schroeder, Y. Fu, F. Zou, V. Battaglia, *J. Power Sources* **2020**, *473*, 228579; b) J. Jang, Y.-T. Chen, G. Deysher, D. Cheng, S.-Y. Ham, A. Cronk, P. Ridley, H. Yang, B. Sayahpour, B. Han, *ACS Energy Lett.* **2022**, *7*, 2531–2539.

[27] Z. Zhang, X. Wang, Y. Bai, C. Wu, *Green Energy & Environ.* **2022**, *7*, 606–635.

[28] a) K. Moyer, R. Carter, T. Hanken, A. Douglas, L. Oakes, C. L. Pint, *Mater. Sci. Eng. B* **2019**, *241*, 42–47; b) P. Zhu, D. Gastol, J. Marshall, R. Sommerville, V. Goodship, E. Kendrick, *J. Power Sources* **2021**, *485*, 229321.
[29] Y.-T. Cheng, M. W. Verbrugge, *J. Power Sources* **2009**, *190*, 453–460.
[30] a) R. Purkayastha, R. McMeeking, *Comput. Mater. Sci.* **2013**, *80*, 2–14; b) J. C. Stallard, L. Wheatcroft, S. G. Booth, R. Boston, S. A. Corr, M. F. De Volder, B. J. Inkson, N. A. Fleck, *Joule* **2022**, *6*, 984–1007.
[31] Z. Ning, G. Li, D. L. Melvin, Y. Chen, J. Bu, D. Spencer-Jolly, J. Liu, B. Hu, X. Gao, J. Perera, *Nature* **2023**, *618*, 287–293.
[32] a) X. Ji, X. Dai, F. Wu, H. Jin, *ACS Sustainable Chem. Eng.* **2022**, *10*, 9850–9859; b) R. D. Lahiru Sandaruwan, L. Cong, L. Ma, S. Ma, H. Wang, *ACS Appl. Mater. Interfaces.* **2021**, *13*, 13264–13272.
[33] S. Jo, J. Han, S. Seo, O. S. Kwon, S. Choi, J. Zhang, H. Hyun, J. Oh, J. Kim, J. Chung, *Adv. Mater.* **2023**, *35*, 2207076.
[34] F. P. McGrogan, Y.-M. Chiang, K. J. Van Vliet, *J. Electroceram.* **2017**, *38*, 215–221.
[35] a) T. Tian, L.-L. Lu, Y.-C. Yin, Y.-H. Tan, T.-W. Zhang, F. Li, H.-B. Yao, *Small* **2022**, *18*, 2106898; b) J.-Y. Piao, Y.-G. Sun, S.-Y. Duan, A.-M. Cao, X.-L. Wang, R.-J. Xiao, X.-Q. Yu, Y. Gong, L. Gu, Y. Li, Z.-J. Liu, Z.-Q. Peng, R.-M. Qiao, W.-L. Yang, X.-Q. Yang, J. B. Goodenough, L.-J. Wan, *Chem* **2018**, *4*, 1685–1695.
[36] C.-a. Lin, S.-k. Lin, *J. Energy Storage* **2024**, *83*, 110637.

Manuscript received: November 21, 2024
Accepted manuscript online: February 4, 2025
Version of record online: ■■, ■■

Research Article

Single-Crystal Cathodes

H. Shin, A. Ndukwe, T. Kim, J. H. Lee,*
G. Li,* H. J. Lee* ——— **e202422726**

Mitigating Diffusion-Induced Intragranular Cracking in Single-Crystal $LiNi_{0.5}Mn_{1.5}O_4$ via Extended Solid-Solution Behavior

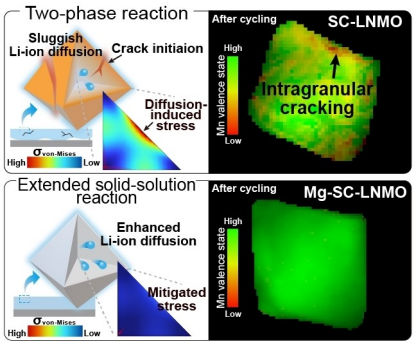

This study outlines a design strategy to enhance the mechanical integrity of single-crystal LNMO cathodes by extending solid-solution behavior. Combined experimental and modeling approaches identify stress distribution within the crystal and demonstrate the role of Mg doping in mitigating intragranular cracking.